Astrodynamics Vol. 8, No. 4, 613–631, 2024 https://doi.org/10.1007/s42064-024-0207-7

Minimum-time rendezvous for Sun-facing diffractive solar sails with diverse deflection angles

Yin Chu[1], **Shengping Gong**[2](✉)

1. School of Aerospace Engineering, Tsinghua University, Beijing 100084, China
2. School of Astronautics, Beihang University, Beijing 100084, China

ABSTRACT

This paper investigates the heliocentric time-optimal rendezvous performance of Sun-facing diffractive solar sails with various deflection angles and acceleration capabilities. Diffractive solar sails, which generate tangential radiation pressure force, are proposed and schematically designed to achieve diverse radiation pressure distributions. The radiation pressure force model and the time-optimal control problem for these innovative Sun-facing diffractive solar sails are established. Utilizing an indirect method and the optimal control law, we explore typical heliocentric rendezvous scenarios to assess the variational trends of transfer time in relation to different deflection angles and acceleration capabilities. The results for Sun-facing diffractive sails in specific rendezvous missions are compared to reflective sails with the same area-to-mass ratio, focusing on transfer trajectory and attitude control. Our findings reveal that diffractive sails exhibit significant advantages over reflective sails, particularly in the context of normal acceleration, paving the way for more efficient space exploration.

KEYWORDS

solar sailing
heliocentric rendezvous
diffractive sail
trajectory design and optimization

Research Article

Received: 9 December 2023
Accepted: 24 February 2024

1 Introduction

A solar sail is a propellantless spacecraft that is propelled by the radiation pressure force due to the momentum exchange between solar photons and the sail surface. Utilizing the continuously available light from the Sun to provide continuous acceleration, though with small magnitude, a solar sail can achieve very high velocity, which is of great promise to turn interstellar travel into reality. Such spacecraft has brought about researchers' interests since the 20th century [1, 2]. This "star-sailing" dream of using a solar sail is becoming a practice since the first successful flying solar sail, the Japanese Space Exploration Agency's Interplanetary Kite-craft spacecraft IKAROS [3–5]. Afterward, a lot of practical missions, like LightSail-1 (Planetary Society) [6], LightSail-2 (Planetary Society) [7], and NanoSail-D2 (NASA) [8], have validated the feasibility of solar sails.

With the development of techniques associated with the optical materials and the fabrication of large-area thin films [9], important yet challenging missions, such as interplanetary transfer missions [10–24] and periodic orbit missions [25–36], and some novel non-conventional orbit missions, such as pole observer missions [37–40] and reversal orbit missions [41, 42], are becoming practical with high-performance solar sails [43–45]. In these missions, the heliocentric transfer phase to reach the target or the working orbit has always been a research hotspot due to its indispensability. Unlike traditional chemical propulsion, the solar sail's transfer mission is primarily designed to use the shortest time. Accordingly, some researchers focus on the strategies, such as indirect methods [46–50], shape-based methods [51], deep neural networks [22], and Q-law [24], to calculate the time-optimal steering law for solar sails, especially for conventional reflective solar sails. However, the conventional reflective solar sail requires shifting the sail surface's attitude relative to the Sun to realize the transfer because of its inherent disadvantage that it can

✉ gongsp@buaa.edu.cn

Nomenclature

a_0	characteristic acceleration
$\boldsymbol{a}_{\mathrm{s}}$	solar radiation pressure induced acceleration
A	sail surface area (m^2)
c	speed of light in vacuum
$\hat{\boldsymbol{e}}_r$, $\hat{\boldsymbol{e}}_h$, $\hat{\boldsymbol{e}}_t$	orbital frame unit vectors
$\hat{\boldsymbol{e}}_x$, $\hat{\boldsymbol{e}}_y$, $\hat{\boldsymbol{e}}_z$	heliocentric frame unit vectors
H	Hamiltonian function
I_{s}	solar constant ($\mathrm{kW/m}^2$)
J	objective function
$\tilde{m}$	spacecraft total mass (kg)
$\hat{\boldsymbol{n}}$, $\hat{\boldsymbol{p}}$	unit vectors normal and perpendicular to the sail surface
r_{e}	Earth–sail distance (AU)
$\boldsymbol{r}$, r	sail position vector, Sun–sail distance (AU)
SRP	abbreviation of solar radiation pressure
t_f	fight time (day)
$\boldsymbol{v}$	sail velocity vector (AU/day)
v_x, v_y, v_z	sail velocity components in $\hat{\boldsymbol{e}}_x$, $\hat{\boldsymbol{e}}_y$, and $\hat{\boldsymbol{e}}_z$ directions (AU)
x, y, z	sail position components in $\hat{\boldsymbol{e}}_x$, $\hat{\boldsymbol{e}}_y$, and $\hat{\boldsymbol{e}}_z$ directions (AU)
α	sail clock angle (deg)
δ	solar radiation pressure acceleration's distribution parameter
ϵ	sail area-to-mass ratio (m^2/kg)
η_n, η_p	components of $\boldsymbol{\eta}$
$\boldsymbol{\eta}$	photon momentum transfer efficiency vector
γ	sail pitch angle (deg)
λ_0	weight constant
$\boldsymbol{\lambda}_r$, $\boldsymbol{\lambda}_v$	co-state vectors associated with position and velocity vectors
μ	solar gravitational constant
$\boldsymbol{\Psi}$	state constraint
θ_o	beam's deflection angle (deg)

only generate the radiation pressure force normal to the sail surface. Such varied attitude configuration of the reflective sail not only lowers the solar usage efficiency but also adds mass and complexity to the system due to the additional attitude adjustment devices, like control vanes [52–55], sliding masses [56–58], and reflectivity control devices [59–61]. Therefore, enhanced solar sails which can maintain a Sun-facing attitude during transfers and the corresponding time-optimal steering laws are worthy of investigation.

Recognizing the limitations of conventional reflective solar sails, researchers have turned their attention to innovative optical materials and microstructures. These advancements aim to create alternatives to reflective sails, enabling the generation of tangential radiation pressure force. Swartzlander *et al.* [62–66] were pioneers in this field, conceptualizing and designing a diffractive solar sail using metamaterial films to generate tangential radiation pressure when facing the Sun. Their concept has been supported by various ground test verifications. Building on this, our research introduces a novel liquid crystal diffraction sail, composed of liquid crystal-phased arrays [67]. This design not only generates tangential radiation pressure force but also allows for electric modulation of the thrust. In parallel, Firuzi and Gong [68] have explored the use of micro-prism arrays to produce significant tangential radiation pressure at near-normal radiation incidence. They further developed a gradient-index solar sail using a transformation optics approach for enhanced beam steering and performance [69]. These innovative sails, harnessing the potential of rapidly advancing optical materials, represent a significant technological leap. However, in actual orbit missions, the advantage of these advanced sails compared with the conventional reflective sail is in the lack of research. These emerging models, though still in its infancy, has sparked interest in orbit design research. Studies are increasingly focusing on its application in interplanetary transfer orbits [70–72] and its potential for the solar polar imager mission [40] as well as the Earth polar observation mission [73].

Our study builds upon the work of Quarta *et al.* [71, 72], who investigated time-optimal transfers of ideal diffractive sails in orbit-to-orbit interplanetary missions. We extend this research to address the complexities of precise rendezvous problems, analyzing various deflection angles to find the optimal configuration for specific missions. Unlike previous studies, which compared diffractive and reflective sails under similar acceleration conditions, our approach uses sails with the same area-to-mass ratio, providing a fairer comparison and deeper insight into the efficiencies of diffractive sails in interplanetary exploration. In this paper, the diffractive sail, which can generate tangential radiation pressure force, is proposed and schematically designed to realize the radiation pressure distribution as diverse as possible. The corresponding theoretical radiation pressure acceleration model is established in the sail's local coordinate system and the orbital coordinate

system. Using a mathematical model set in a rectangular coordinate frame and an indirect method, we tackle the minimum-time rendezvous problem, deriving an optimal control law for Sun-facing diffractive sails. Then, we explore two types of heliocentric rendezvous missions: planetary rendezvous and near-Earth asteroid rendezvous, using Sun-facing diffractive sails with varying deflection angles and acceleration capabilities. Through a parametric study, we assess transfer time under different deflection angles and acceleration conditions to select the most suitable diffractive sail for each mission. Finally, we compare the optimal solutions and steering laws of the chosen diffractive sails in Sun-facing attitude with conventional reflective sails, highlighting the advantages of diffractive sails in heliocentric rendezvous missions.

The structure of this paper is as follows: Section 2 introduces the dynamical model and proposes two types of diffractive solar sails with varying deflection angles for diverse radiation pressure distributions, along with their acceleration models. Section 3 analyzes the time-optimal control problem for Sun-facing diffractive sails in rendezvous missions and derives the optimal control law. In Section 4, we examines typical planetary and near-Earth asteroid rendezvous missions for diffractive sails with different deflection angles and acceleration capabilities. The best diffractive sail with the most suitable deflection angle is picked and compared with the attitude-variable reflective sail for each mission. Section 5 compares the optimal solutions and steering laws of the chosen diffractive sails in Sun-facing attitude with conventional reflective sails of the same area-to-mass ratio for specific missions. Finally, Section 6 presents our conclusions.

2 Mathematical model

The sunlight deflection angle determines the radiation pressure distribution for Sun-facing diffractive sails. To explore the optimal heliocentric rendezvous trajectories for these sails under varied radiation pressure distributions, let us first clarify the orbital dynamics and radiation pressure acceleration model of the diffractive sail with different deflection angles.

2.1 Dynamical model

For the heliocentric transfer orbits of solar sails, we consider a two-body system consisting of the Sun and the sail, beyond the gravitational influence of other bodies such as the Earth. Here, we use the general location vector $\boldsymbol{r}$ and velocity vector $\boldsymbol{v}$, as well as the osculating orbital elements $(a, e, i, \Omega, \omega, \theta)$ to depict the state of the sail, as illustrated in Fig. 1. In general, with only the gravitational force and radiation force of the Sun in consideration, the state equations of a solar sail in a heliocentric orbit are simply described by

$$\begin{cases} \dot{\boldsymbol{r}} = \boldsymbol{v} \\ \dot{\boldsymbol{v}} = -\dfrac{\mu}{r^3}\boldsymbol{r} + \boldsymbol{a}_{\mathrm{s}} \end{cases} \tag{1}$$

where r is the distance between the sailcraft and the Sun, μ is a solar gravitational constant, and $\boldsymbol{a}_{\mathrm{s}}$ is the solar radiation pressure (SRP) acceleration vector acting on the sail.

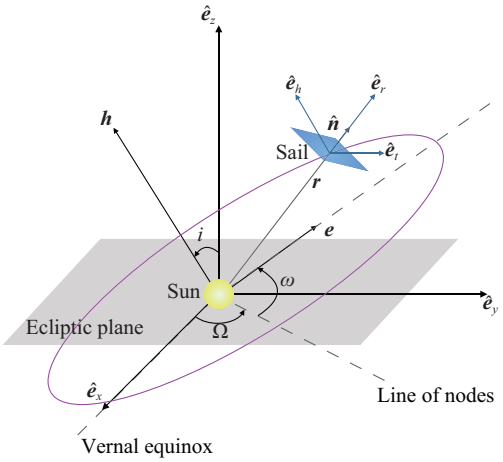

Fig. 1 Heliocentric reference frame.

For this problem, we choose the unit of length to be the distance between the Sun and Earth, i.e., 1 AU, and the unit of time to be 1 day. Let $(\hat{\boldsymbol{e}}_x, \hat{\boldsymbol{e}}_y, \hat{\boldsymbol{e}}_z)$ be a set of right-handed, orthonormal vectors of the heliocentric ecliptic rectangular coordinate reference frame. Then, the sailcraft's position and velocity vectors can be expressed as

$$\begin{cases} \boldsymbol{r} = x\hat{\boldsymbol{e}}_x + y\hat{\boldsymbol{e}}_y + z\hat{\boldsymbol{e}}_z \\ \boldsymbol{v} = v_x\hat{\boldsymbol{e}}_x + v_y\hat{\boldsymbol{e}}_y + v_z\hat{\boldsymbol{e}}_z \end{cases} \tag{2}$$

Because the SRP acceleration of the sail is closely related to the intensity and direction of sunlight, it is complicated to express the SRP acceleration in the rectangular coordinate reference system. Here, we adapt a set of basic vectors $(\hat{\boldsymbol{e}}_r, \hat{\boldsymbol{e}}_t, \hat{\boldsymbol{e}}_h)$ of the osculating orbital plane to clarify the sail's SRP acceleration $\boldsymbol{a}_{\mathrm{s}}$, as illustrated in Fig. 1. The relationship between the orbital coordinate unit vectors $(\hat{\boldsymbol{e}}_r, \hat{\boldsymbol{e}}_t, \hat{\boldsymbol{e}}_h)$ and the state vectors of the sail is

$$\begin{cases} \hat{\boldsymbol{e}}_r = \dfrac{\boldsymbol{r}}{r} \\ \hat{\boldsymbol{e}}_h = \dfrac{\boldsymbol{r}\times\boldsymbol{v}}{\|\boldsymbol{r}\times\boldsymbol{v}\|} \\ \hat{\boldsymbol{e}}_t = \hat{\boldsymbol{e}}_h \times \hat{\boldsymbol{e}}_r \end{cases} \tag{3}$$

By expanding the above expressions, the transformation from rectangular coordinate system $(\hat{\boldsymbol{e}}_x, \hat{\boldsymbol{e}}_y, \hat{\boldsymbol{e}}_z)$ to orbital coordinate system $(\hat{\boldsymbol{e}}_r, \hat{\boldsymbol{e}}_t, \hat{\boldsymbol{e}}_h)$ can be obtained, as Eq. (4)

$$\begin{bmatrix} \hat{\boldsymbol{e}}_r \\ \hat{\boldsymbol{e}}_h \\ \hat{\boldsymbol{e}}_t \end{bmatrix} = \begin{bmatrix} \frac{x}{r} & \frac{yv_z - zv_y}{h} & \frac{(x^2+y^2)v_x - x(yv_y+zv_z)}{rh} \\ \frac{y}{r} & \frac{zv_x - xv_z}{h} & \frac{(x^2+z^2)v_y - y(xv_x+zv_z)}{rh} \\ \frac{z}{r} & \frac{xv_y - yv_x}{h} & \frac{(x^2+y^2)v_z - z(xv_x+yv_y)}{rh} \end{bmatrix}^{\mathrm{T}} \begin{bmatrix} \hat{\boldsymbol{e}}_x \\ \hat{\boldsymbol{e}}_y \\ \hat{\boldsymbol{e}}_z \end{bmatrix} \tag{4}$$

where $h = \|\boldsymbol{r}\times\boldsymbol{v}\|$ is the angular momentum magnitude. The specific expressions of the SRP acceleration components expressed in the orbital coordinate system $(\hat{\boldsymbol{e}}_r, \hat{\boldsymbol{e}}_h, \hat{\boldsymbol{e}}_t)$ will be illustrated in Section 2.2.

2.2 Solar radiation pressure acceleration model

The acceleration produced by the solar radiation pressure for a solar sail is determined by the solar irradiance $I(r)$, sail area A, sail mass $\tilde{m}$, and momentum transfer efficiency vector $\boldsymbol{\eta}$. The general expression of the SRP acceleration could be written as Eq. (5):

$$\boldsymbol{a}_{\mathrm{s}} = a_0 \boldsymbol{\eta} \frac{r_{\mathrm{e}}^2}{r^2} \tag{5}$$

where $r_{\mathrm{e}} = 1$ AU. In Eq. (5), a_0 mainly determines the acceleration capability of the sail, called the characteristic acceleration. a_0 is solely related to the sails' area-to-mass ratio ϵ, having the expression as Eq. (6):

$$a_0(\epsilon) = \frac{I_{\mathrm{s}}\epsilon}{c} \tag{6}$$

where $I_{\mathrm{s}} = 1.37\ \mathrm{kW/m^2}$ is the solar constant and c is the speed of light. The value of a_0 is equal to the magnitude of SRP acceleration for a fully absorbed sail with the same area-to-mass ratio ϵ at the location in 1 AU and the Sun-facing attitude. Equation (6) indicates that the acceleration capability of the sail is proportional to the sail's area-to-mass ratio.

In the general formula of the sail's SRP acceleration Eq. (5), $\boldsymbol{\eta}$ represents the momentum transfer efficiency vector of the sail, determining the utilization efficiency of the sail to the sunlight and the direction of the sail's SRP acceleration. The momentum transfer efficiency vector $\boldsymbol{\eta}$ is mainly related to the optical properties and the attitude of the sail, having the expression as Eq. (7):

$$\boldsymbol{\eta} = \eta_n \hat{\boldsymbol{n}} + \eta_p \hat{\boldsymbol{p}} \tag{7}$$

where $\hat{\boldsymbol{n}}$ represents the direction normal to the sail surface and opposite to the Sun, $\hat{\boldsymbol{p}}$ represents the direction parallel to the sail surface, η_n and η_p respectively represent the normal and tangential components of momentum transfer efficiency for the sail.

In order to specific illustrate the SRP induced acceleration distribution, let the parameter $\delta = \eta_p/\eta_n$ represent the ratio of tangential to normal SRP acceleration to describe the SRP acceleration's distribution. For conventional ideal flat reflective solar sail, only the normal component of SRP acceleration for the sail exists according to the law of reflection. In other words, only the circumstance of $\delta = 0$ could be achieved for the ideal reflective sail. On the contrary, it is capable for diffractive sails to vary the distribution parameter δ in a considerably broad range. Thereby, the diffractive sail can be taken as the realizable model to achieve various SRP acceleration's distributions. For the diffractive sail, beam directional deflection could be achieved by designing an appropriate microstructure of the sail. The deflection angle θ_o could reach as large as 90° with modern optical design and fabrication techniques [64].

Depending on the optical properties of the materials and structures used in the diffractive sail, there exist two cases of beam propagation as depicted in Fig. 2. Type-1 represents the diffractive sail composed of reflection material, and type-2 represents the diffractive sail composed of transmission material. The outgoing beams and incident beams are on the same side for type-1, and on the opposite side for type-2, as depicted in Fig. 2(a) and Fig. 2(b), respectively. Based on the wave-particle duality of the light and momentum exchange principle, the SRP acceleration of the sail and the momentum transfer efficiencies along the normal and tangential directions are as Eq. (8):

$$\begin{aligned} &\boldsymbol{a}_{\mathrm{s}} = a_0 \frac{r_{\mathrm{e}}^2}{r^2}(\eta_n \hat{\boldsymbol{n}} + \eta_p \hat{\boldsymbol{p}}) \\ &\begin{cases} \eta_n = 1 \pm \cos\theta_o \\ \eta_p = \sin\theta_o \end{cases} \end{aligned} \tag{8}$$

and the ratio of tangential to normal SRP acceleration can be calculated as Eq. (9):

$$\delta = \frac{\sin\theta_o}{1 \pm \cos\theta_o} \tag{9}$$

where the plus and minus signs correspond to the reflection-type and transmission-type diffractive sails, respectively.

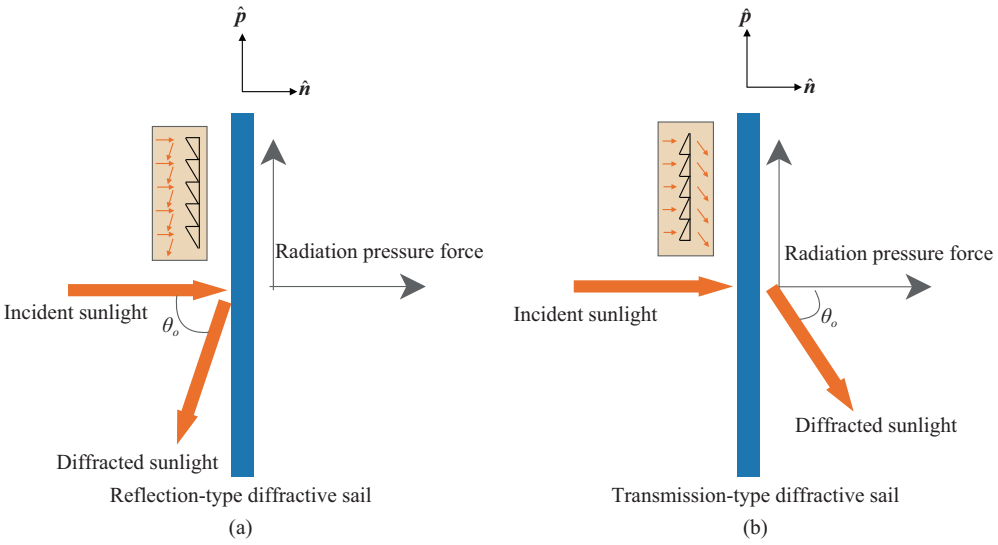

Fig. 2 Schematic diagram of the beam propagation and the SRP force for diffractive solar sail at a Sun-facing attitude.

According to Eq. (9), the relationship between the SRP acceleration's distribution parameter with the deflection angle of beams by diffractive sails is shown in Fig. 3. For reflection-type sails, the distribution parameter ranges from 0 to 1, indicating a dominance of normal SRP acceleration. In contrast, transmission-type sails have a parameter range from 1 to $+\infty$, highlighting the predominance of tangential SRP acceleration. This understanding allows for designing diffractive sails with specific structures and materials to achieve the desired distribution between tangential and normal radiation pressure.

Further analysis, as shown in Fig. 4, explores the relationship between the magnitudes of total SRP acceleration and its components with the beams' deflection angles for both sail types, assuming an area-to-mass ratio of $\epsilon = 150$ m^2/kg. For reflection-type sails, increasing the deflection angle reduces total SRP acceleration, indicating lower sunlight utilization efficiency. Simultaneously, normal SRP acceleration decreases while tangential acceleration increases. Conversely, for transmission-type sails, total SRP acceleration diminishes as the deflection angle decreases, similarly suggesting reduced sunlight efficiency. In this case, both normal and tangential SRP accelerations decrease with a smaller deflection angle. This detailed understanding aids in optimizing diffractive sail design for varying deflection angles.

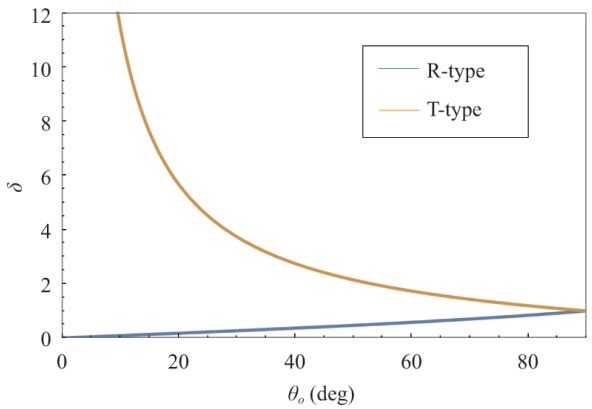

Fig. 3 Relationship between the ratio of tangential to normal SRP acceleration with the beams' deflection angle for two types of diffractive sails.

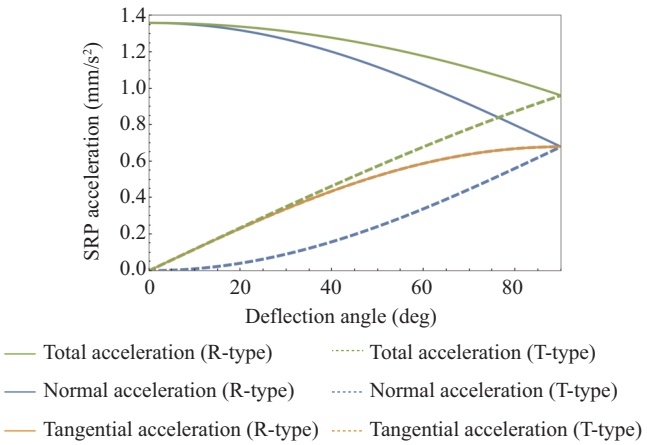

Fig. 4 Relationship between the magnitudes of total SRP acceleration and SRP acceleration components with the beams' deflection angle for two types of diffractive sails.

To explore the diffractive sail's trajectory in

heliocentric transfers, it is necessary to derive the SRP acceleration components along the directions of the orbital coordinate axes $(\hat{\boldsymbol{e}}_r, \hat{\boldsymbol{e}}_t, \hat{\boldsymbol{e}}_h)$. Given the diffractive sail ability to generate tangential SRP acceleration, we focus on the Sun-facing attitude. The direction of SRP acceleration can be controlled by rolling the diffractive grating by an angle α around the normal, making this clock angle a crucial attitude control parameter for sail navigation. By referencing the relationship between the sail local coordinate system $(\hat{\boldsymbol{n}}, \hat{\boldsymbol{p}})$ and the orbital coordinate system $(\hat{\boldsymbol{e}}_r, \hat{\boldsymbol{e}}_t, \hat{\boldsymbol{e}}_h)$, as illustrated in Fig. 5(a), we can expressed the SRP acceleration for the diffractive sail in the orbital coordinate system, as Eq. (10):

$$\boldsymbol{a}_{\mathrm{s}} = a_0 \frac{r_{\mathrm{e}}^2}{r^2}(\eta_n \hat{\boldsymbol{e}}_r + \eta_p \sin\alpha \hat{\boldsymbol{e}}_t + \eta_p \cos\alpha \hat{\boldsymbol{e}}_h) \tag{10}$$

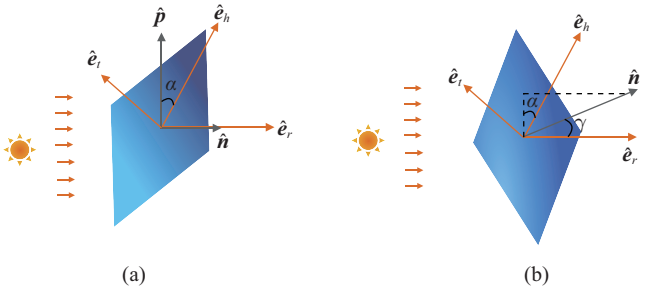

Fig. 5 Schematic diagram of the attitude for the diffractive solar sail and the reflective sail. (a) Diffractive sail with clock angle α. (b) Reflective sail with pitch angle γ and clock angle α.

Let us contrast the SRP acceleration of the diffractive sail with the ideal reflective sail, depicted in Fig. 5(b). For the ideal reflective solar sail, due to the property that it can only generate normal SRP acceleration, we consider the variable attitude with the pitch angle γ and the clock angle α. The SRP acceleration of the ideal reflective sail is expressed as Eq. (11):

$$\boldsymbol{a}_{\mathrm{s}} = 2a_0 \frac{r_{\mathrm{e}}^2}{r^2} \cos^2\gamma(\cos\gamma \hat{\boldsymbol{e}}_r + \sin\gamma \sin\alpha \hat{\boldsymbol{e}}_t + \sin\gamma \cos\alpha \hat{\boldsymbol{e}}_h) \tag{11}$$

Using Eqs. (10) and (11), we compare the solar radiation pressure (SRP) acceleration characteristics of diffractive and reflective sails, as illustrated in the acceleration vector hodograph in Fig. 6. This figure shows the SRP acceleration vector profiles for two types of Sun-facing diffractive sails with different deflection angles and the ideal reflective sail with variable attitude. The SRP acceleration for the Sun-facing diffractive sail and the attitude-variable reflective sail forms a continuous

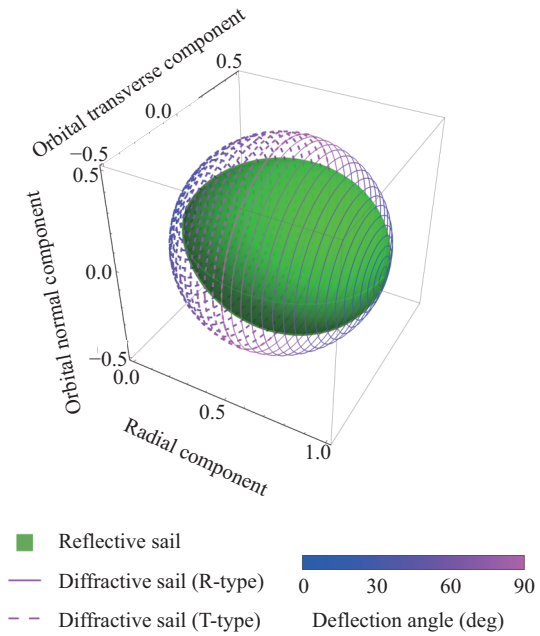

Fig. 6 Hodographs of dimensionless SRP acceleration vectors at 1 AU for diffractive sails (colored lines) with various deflection angles when keeping Sun-facing attitude and the ideal reflective sail (green surface) with variable attitude.

circle curve and a continuous surface, respectively. While the attitude-variable reflective sail has more control dimensions, a diffractive sail with an appropriate deflection angle can always match the reflective sail for each attitude. Notably, when the radial SRP acceleration of the matching diffractive sail aligns with that of the reflective sail, the transverse and orbital normal SRP accelerations of the diffractive sail tend to be higher, which may be beneficial for some heliocentric transfer missions.

3 Trajectory optimization

In order to analyze the heliocentric transfers for the Sun-facing diffractive solar sail with various deflection angles and compare the transfer performance with the conventional reflective sail, we consider an optimal interplanetary transfer problem, where the sail thrust vector is steered in such a way as to minimize the flight time required to transfer the spacecraft from the Earth to the target. It should be noted that launch dates are not included in optimization for reason of studying acceleration components, influence on sailcraft dynamics. For the attitude-variable reflective sail, the mathematical model that gives the optimal transfer trajectories and the corresponding optimal control law of the controllable

pitch angle γ and clock angle α have been detailed in Ref. [13]. This section delves into the time-optimal transfer problem and the optimal control law for the Sun-facing diffractive sail.

The objective function of trajectory optimization for the solar sail is the total time of flight (TOF) as Eq. (12):

$$\min J = \int_0^{t_f} \lambda_0 \mathrm{d}t \tag{12}$$

where λ_0 is a positive weight constant, and t_f is the total time of flight.

Given the above state equation Eq. (1) and the radiation pressure force Eq. (10), the Hamiltonian function of the system is

$$\begin{aligned} H &= \boldsymbol{\lambda}_r \cdot \boldsymbol{v} + \boldsymbol{\lambda}_v \cdot \left[-\frac{\mu}{r^3}\boldsymbol{r} + a_0(\eta_n \hat{\boldsymbol{e}}_r + \eta_p \sin\alpha \hat{\boldsymbol{e}}_t \right. \\ &\quad \left. + \eta_p \cos\alpha \hat{\boldsymbol{e}}_h)\frac{r_\mathrm{e}^2}{r^2}\right] + \lambda_0 \\ &= \boldsymbol{\lambda}_r \cdot \boldsymbol{v} + \boldsymbol{\lambda}_v \cdot (-\mu + a_0\eta_n r_\mathrm{e}^2)\frac{\boldsymbol{r}}{r^3} \\ &\quad + a_0\eta_p \frac{r_\mathrm{e}^2}{r^2}\boldsymbol{\lambda}_v \cdot (\sin\alpha \hat{\boldsymbol{e}}_t + \cos\alpha \hat{\boldsymbol{e}}_h) + \lambda_0 \end{aligned} \tag{13}$$

where $\boldsymbol{\lambda}_r$ and $\boldsymbol{\lambda}_v$ are the co-state vectors associated with the position and velocity vectors, respectively.

Based on Pontryagin's Maximum Principle [74], the optimal control law minimizes the Hamiltonian function. Therefore, we can obtain the optimal control law of the clock angle α^* for the Sun-facing diffractive sail to achieve the minimum time orbit transfer, as Eq. (14):

$$\begin{cases} \sin\alpha^* = -\dfrac{\boldsymbol{\lambda}_v \cdot \hat{\boldsymbol{e}}_t}{\sqrt{(\boldsymbol{\lambda}_v \cdot \hat{\boldsymbol{e}}_t)^2 + (\boldsymbol{\lambda}_v \cdot \hat{\boldsymbol{e}}_h)^2}} \\ \cos\alpha^* = -\dfrac{\boldsymbol{\lambda}_v \cdot \hat{\boldsymbol{e}}_h}{\sqrt{(\boldsymbol{\lambda}_v \cdot \hat{\boldsymbol{e}}_t)^2 + (\boldsymbol{\lambda}_v \cdot \hat{\boldsymbol{e}}_h)^2}} \end{cases} \tag{14}$$

In order to simplify the derivation and calculation of the co-state equations, introduce the parameter $\boldsymbol{\alpha}$ to substitute $(\sin\alpha\hat{\boldsymbol{e}}_t + \cos\alpha\hat{\boldsymbol{e}}_h)$. Accordingly, the parameter $\boldsymbol{\alpha}$ should be a unit vector and perpendicular to $\boldsymbol{r}$. Then, the Hamiltonian function can be written as

$$H = \boldsymbol{\lambda}_r \cdot \boldsymbol{v} + \boldsymbol{\lambda}_v \cdot \left(-\mu + a_0\eta_n r_\mathrm{e}^2\right)\frac{\boldsymbol{r}}{r^3} + a_0\eta_p \frac{r_\mathrm{e}^2}{r^2}\boldsymbol{\lambda}_v \cdot \boldsymbol{\alpha} \tag{15}$$

To minimize the Hamiltonian function, $\boldsymbol{\alpha}$'s direction should be opposite to the component vector of $\boldsymbol{\lambda}_v$ on the plane perpendicular to $\boldsymbol{r}$, that is,

$$\boldsymbol{\alpha}^* = -\frac{\boldsymbol{\lambda}_v - \frac{\boldsymbol{\lambda}_v \cdot \boldsymbol{r}}{r^2}\boldsymbol{r}}{\left\|\boldsymbol{\lambda}_v - \frac{\boldsymbol{\lambda}_v \cdot \boldsymbol{r}}{r^2}\boldsymbol{r}\right\|} \tag{16}$$

where $\boldsymbol{\alpha}^*$ is the optimal law of $\boldsymbol{\alpha}$ corresponding to the optimal control angle α.

Then, we can obtain the Euler–Lagrange equations via the derivative of the state variable by the Hamilton function as

$$\begin{cases} \dot{\boldsymbol{\lambda}}_r = -\dfrac{\partial H}{\partial \boldsymbol{r}} = \left(-\mu + a_0\eta_n r_\mathrm{e}^2\right)\left[-\dfrac{\boldsymbol{\lambda}_v}{r^3} + \dfrac{3(\boldsymbol{\lambda}_v \cdot \boldsymbol{r})\boldsymbol{r}}{r^5}\right] \\ \qquad + 2a_0\eta_p \dfrac{r_\mathrm{e}^2}{r^4}(\boldsymbol{\lambda}_v \cdot \boldsymbol{\alpha}^*)\boldsymbol{r} \\ \dot{\boldsymbol{\lambda}}_v = -\dfrac{\partial H}{\partial \boldsymbol{v}} = -\boldsymbol{\lambda}_r \end{cases} \tag{17}$$

Considering the rendezvous problem that the initial and terminal states of the solar sail are the same as that of the departure and arrival celestial body, the state constrains can be expressed as

$$\begin{cases} \boldsymbol{\Psi}(0) = \begin{Bmatrix} \boldsymbol{r}(0) - \boldsymbol{r}_0(0) \\ \boldsymbol{v}(0) - \boldsymbol{v}_0(0) \end{Bmatrix} = \boldsymbol{0} \\ \boldsymbol{\Psi}(t_f) = \begin{Bmatrix} \boldsymbol{r}(t_f) - \boldsymbol{r}_f(t_f) \\ \boldsymbol{v}(t_f) - \boldsymbol{v}_f(t_f) \end{Bmatrix} = \boldsymbol{0} \end{cases} \tag{18}$$

where $\boldsymbol{r}_0$ and $\boldsymbol{v}_0$ are the position and velocity of the departure celestial body, and $\boldsymbol{r}_f$ and $\boldsymbol{v}_f$ are the position and velocity of the arrival celestial body, respectively. It should be noted that the arrival state constraints is the target celestial body's actual position and velocity at the final time based on its ephemerides.

According to the optimal control theory, the boundary conditions satisfy the transversality conditions as

$$\begin{cases} \boldsymbol{\lambda}_r(0) = -\boldsymbol{\gamma}_0 \cdot \dfrac{\partial \boldsymbol{\Psi}}{\partial \boldsymbol{r}(0)} = -\boldsymbol{\gamma}_{r0} \\ \boldsymbol{\lambda}_v(0) = -\boldsymbol{\gamma}_0 \cdot \dfrac{\partial \boldsymbol{\Psi}}{\partial \boldsymbol{v}(0)} = -\boldsymbol{\gamma}_{v0} \\ \boldsymbol{\lambda}_r(t_f) = -\boldsymbol{\gamma}_f \cdot \dfrac{\partial \boldsymbol{\Psi}}{\partial \boldsymbol{r}(t_f)} = -\boldsymbol{\gamma}_{rf} \\ \boldsymbol{\lambda}_v(t_f) = -\boldsymbol{\gamma}_f \cdot \dfrac{\partial \boldsymbol{\Psi}}{\partial \boldsymbol{v}(t_f)} = -\boldsymbol{\gamma}_{vf} \end{cases} \tag{19}$$

where $\boldsymbol{\gamma}_0 \triangleq (\boldsymbol{\gamma}_{r0}; \boldsymbol{\gamma}_{v0})$ and $\boldsymbol{\gamma}_f \triangleq (\boldsymbol{\gamma}_{rf}; \boldsymbol{\gamma}_{vf})$ are Lagrange multipliers related to the initial and final time constraints, respectively. Additionally, the final stationary condition is given by

$$H(t_f) = -\boldsymbol{\gamma}_f \cdot \frac{\partial \boldsymbol{\Psi}}{\partial t_f} = 0 \tag{20}$$

Then, we use the numerical indirect shooting method [75] to solve the associated two-point boundary value problem. By guessing the initial co-state vectors and the overall transfer time, we can obtain the arrival states and co-states of the sail by integrating Eqs. (1) and (17). These values will be used in an iteration to check the optimality conditions, which have been specifically discussed in Ref. [22]. In this way, we can find the

appropriate initial co-state vectors and transfer time, integrating with which both the state constraints and the optimality conditions can be satisfied. Then, the optimal control law of the clock angle α can be calculated through Eq. (14). Adapting the numerical optimization method discussed above, we can obtain the time-optimal rendezvous for the Sun-facing diffractive solar sail with given deflection angles.

4 Parametric study for rendezvous missions

In this section, we analyze the minimum-time rendezvous for diffractive sails in two types of heliocentric missions: planetary and near-Earth asteroid rendezvous. We examine diffractive sails with various deflection angles and different area-to-mass ratios, focusing on identifying the most suitable deflection angle for each mission based on how it affects transfer time.

Here, three different acceleration capabilities of diffractive sails are considered to encompass different maneuverability performances:

1) High acceleration capability with an area-to-mass ratio of 150 m^2/kg and the characteristic acceleration of 0.68 mm/s^2. Currently, such a sail is limited by the availability of ultra-thin, super-lightweight film materials, but it represents a potential future development.

2) Moderate acceleration capability with an area-to-mass ratio of 50 m^2/kg and the characteristic acceleration of 0.227 mm/s^2. Advances in optical materials, including meta-materials and liquid crystal polymers, have facilitated the creation of lightweight and thin polarization converters and diffraction gratings suitable for such sails [76–78].

3) Low acceleration capability using conventional membrane materials with an area-to-mass ratio of 25 m^2/kg and the characteristic acceleration of 0.113 mm/s^2.

We then apply an indirect method to numerically solve the time-optimal rendezvous problem for specific missions, considering diffractive sails with these three levels of acceleration capabilities and various deflection angles.

For the planetary rendezvous mission, we focus on Mercury and Mars, with Mercury requiring a decrease and Mars an increase in the orbital semi-major axis relative to the Earth.

For the Earth-to-Mercury mission, we assume departure at Modified Julian Date (MJD) 58,086.7, with orbital elements detailed in Table 1. Figure 7 presents the optimal transfer time for Sun-facing diffractive sails with varying deflection angles and three acceleration capabilities, alongside the optimal time for a reflective sail with the same area-to-mass ratio.

For the Earth-to-Mars mission, the assumed departure is at MJD 57,800, with orbital elements in Table 2. Figure 8 shows the optimal transfer time for Sun-facing diffractive sails with varying deflection angles and three

Table 1 Orbit elements of the Earth at departure time for Mercury rendezvous mission

MJD	a (AU)	e	i (rad)	Ω (rad)	ω (rad)	θ (rad)
58,086.7	0.9994	0.0164	2.2×10^{-5}	2.58483	5.52899	5.62916

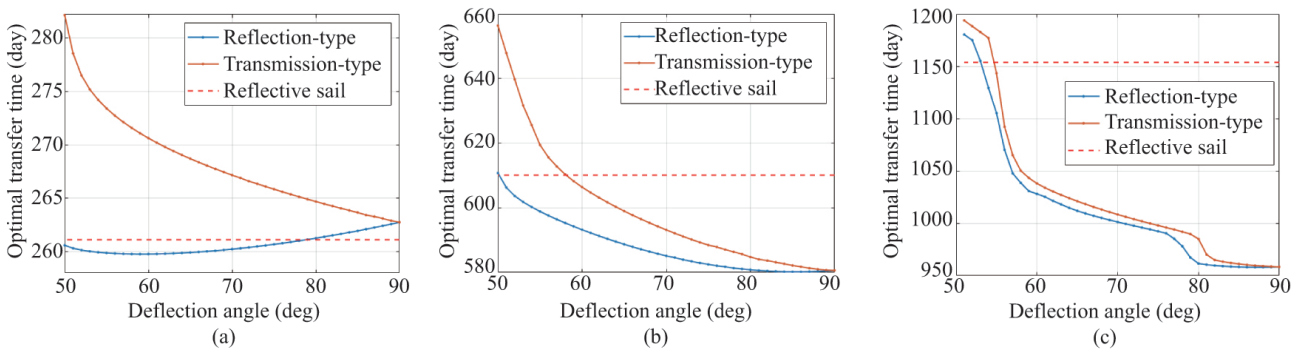

Fig. 7 Optimal transfer time from the Earth to Mercury for Sun-facing diffractive sails with various deflection angles (solid lines) and the attitude-variable reflective sail with the same area-to-mass ratio(dashed line). (a) High acceleration capability case ($\epsilon = 150$ m^2/kg). (b) Moderate acceleration capability case ($\epsilon = 50$ m^2/kg). (c) Low acceleration capability case ($\epsilon = 25$ m^2/kg).

Table 2 Orbit elements of the Earth at departure time for Mars rendezvous mission

MJD	a (AU)	e	i (rad)	Ω (rad)	ω (rad)	θ (rad)
57,800	0.999537	0.016605	2.2×10^{-5}	3.58818	4.45914	0.806124

Table 3 Orbit elements of the Earth at departure time for Apophis rendezvous mission

MJD	a (AU)	e	i (rad)	Ω (rad)	ω (rad)	θ (rad)
57,984.5	1.00078	0.016605	2.2×10^{-5}	2.8311	5.22412	3.92577

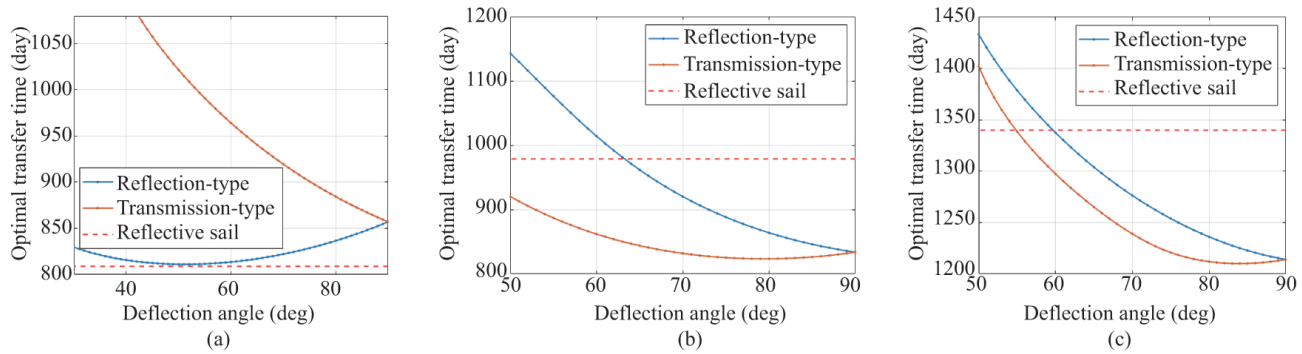

Fig. 8 Optimal transfer time from the Earth to Mars for Sun-facing diffractive sails with various deflection angles (solid lines) and the attitude-variable reflective sail with the same area-to-mass ratio (dashed line). (a) High acceleration capability case ($\epsilon = 150$ m^2/kg). (b) Moderate acceleration capability case ($\epsilon = 50$ m^2/kg). (c) Low acceleration capability case ($\epsilon = 25$ m^2/kg).

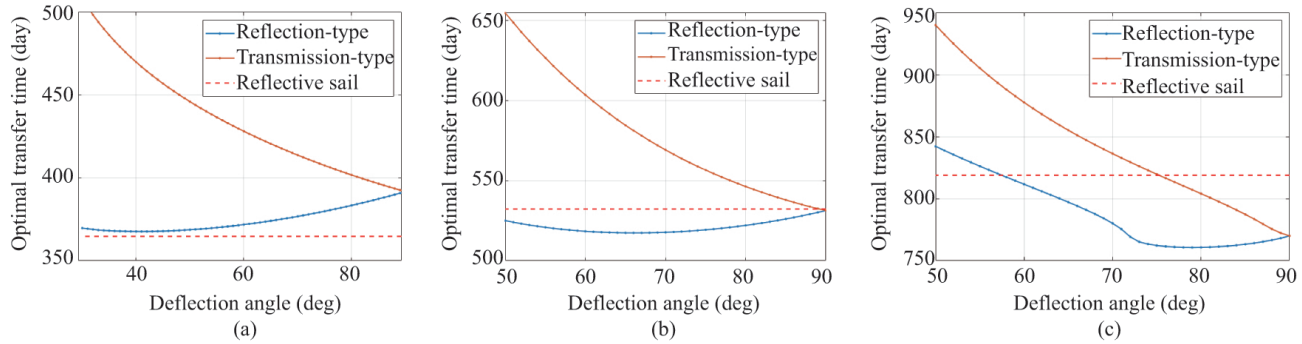

Fig. 9 Optimal transfer time from the Earth to Apophis for Sun-facing diffractive sails with various deflection angles (solid lines) and the attitude-variable reflective sail with the same area-to-mass ratio (dashed line). (a) High acceleration capability case ($\epsilon = 150$ m^2/kg). (b) Moderate acceleration capability case ($\epsilon = 50$ m^2/kg). (c) Low acceleration capability case ($\epsilon = 25$ m^2/kg).

acceleration capabilities, alongside the optimal time for a reflective sail with the same area-to-mass ratio.

For the near-Earth asteroid rendezvous mission, we select asteroid (99942) Apophis, whose orbital semi-major axis is similar to the Earth's, necessitating phase regulation. Whenever it approaches and leaves the Sun, its orbit will intersect the Earth's orbit, which is worth exploring. The departure for the Apophis mission is assumed at MJD 57,984.5, with details in Table 3. Figure 9 illustrates the optimal transfer time for Sun-facing diffractive sails to Apophis, comparing different deflection angles, acceleration capabilities, and a reflective sail with equivalent area-to-mass ratio.

Figures 7, 8, and 9 reveal how the optimal transfer time varies with deflection angle for diffractive sails of three acceleration capabilities in Mercury, Mars, and Apophis rendezvous missions.

1) High acceleration capability: Reflection-type diffractive sails outperform transmission-type in all missions, with optimal transfer time slightly fluctuating with deflection angle changes. Transmission-type sails show a rapid increase in transfer time as the deflection

angle decreases.

2) Reflection-type sails are more efficient for Mercury and Apophis rendezvous, while transmission-type sails excel in Mars rendezvous. For Mercury rendezvous, transfer time generally increases with decreasing deflection angle for both sail types. In Mars rendezvous, transfer time for reflection-type sails increases with decreasing deflection angle, whereas for transmission-type sails, it initially decreases, reaching a minimum at 80 deg. For Apophis rendezvous, reflection-type sails show minor influence of deflection angle on transfer time, whereas transmission-type sails experience a rapid increase.

3) Low acceleration capability: Transfer time generally increases with deflection angle decrease for both sail types in all missions. Reflection-type sails are more effective for Mercury and Apophis rendezvous, while transmission-type sails excel in Mars rendezvous.

From Fig. 7, Fig. 8, and Fig. 9, we can also observe the comparison of the optimal transfer time for the reflective sail with the diffractive sail at the same area-to-mass ratio. For the sails with the area-to-mass ratio of $\epsilon = 150$ m^2/kg, the shortest transfer time of the diffractive sail is almost as short as that of the reflective sail. For the sails with the area-to-mass ratio of $\epsilon = 50$ m^2/kg and $\epsilon = 25$ m^2/kg, the transfer time of the reflective sail is quite longer than that of the diffractive sail with the most deflection angles in all three rendezvous missions.

Additionally, by comparing the variation of the optimal transfer time for the diffractive sail with the deflection angle under three acceleration capabilities in the three rendezvous missions, we can preliminarily observe the characteristics of transfer time and optimal deflection angle for different area-to-mass ratios of sails. (1) Lower area-to-mass ratio sails have longer transfer time due to reduced acceleration capability. (2) The difference in transfer time between reflection-type and transmission-type diffractive sails decreases with lower area-to-mass ratios. This is because the gravitational force of the sun on these low area-to-mass ratio sails is much greater than the radiation pressure force component along the sun-line, which is the only force difference between two types of sails. (3) Optimal deflection angle for lower area-to-mass ratio sails is closer to 90 deg. (4) Diffractive sails are more advantageous than reflective sails, especially at lower area-to-mass ratios.

Tables 4, 5, and 6 present the optimal structure parameters and transfer time for the most suitable diffractive sails for Mercury, Mars, and Apophis

Table 4 Comparison of the most suitable diffractive sail and the reflective sail for Mercury rendezvous mission

Sail type (best diffractive sail or ideal reflective sail)	ϵ (m^2/kg)	$\lvert\boldsymbol{a}_s\rvert$ (mm/s^2)	Best deflection angle (deg)	Transfer time (day)	(year)	Flight time difference (day)
High acceleration capability:						
Reflection-type diffractive sail	150	1.1841	59	259.8	0.711	−1.3
Ideal reflective sail	150	1.3605	—	261.1	0.715	—
Moderate acceleration capability:						
Reflection-type diffractive sail	50	0.3344	85	580.2	1.588	−29.9
Ideal reflective sail	50	0.4535	—	610.1	1.670	—
Low acceleration capability:						
Reflection-type diffractive sail	25	0.1645	87	957.9	2.623	−195.9
Ideal reflective sail	25	0.2268	—	1153.8	3.159	—

Table 5 Comparison of the most suitable diffractive sail and the reflective sail for Mars rendezvous mission

Sail type (best diffractive sail or ideal reflective sail)	ϵ (m^2/kg)	$\lvert\boldsymbol{a}_s\rvert$ (mm/s^2)	Best deflection angle (deg)	Transfer time (day)	(year)	Flight time difference (day)
High acceleration capability:						
Reflection-type diffractive sail	150	1.228	51	811.1	2.221	+2.1
Ideal reflective sail	150	1.3605	—	809.0	2.215	—
Moderate acceleration capability:						
Transmission-type diffractive sail	50	0.2915	80	823.4	1.588	−155.2
Ideal reflective sail	50	0.4535	—	978.6	2.679	—
Low acceleration capability:						
Transmission-type diffractive sail	25	0.1517	84	1210.1	3.313	−129.9
Ideal reflective sail	25	0.2268	—	1340.0	3.669	—

rendezvous missions, compared with reflective sails of the same area-to-mass ratio. It can be seen that the reflection-type diffractive sail always outperform the transmission-type diffractive sail regardless of the acceleration capability of the sail for both the Mercury and Apophis rendezvous missions. However, for the Mars rendezvous mission, the transmission-type diffractive sail outperforms when the acceleration capability is limited. As the acceleration capability decreases, larger deflection angle is expected to achieve faster transfer to these three rendezvous objects. Compared with the ideal reflective sail at the same area-to-mass ratio, although the SRP acceleration's magnitude for the diffractive sail is not as large as that for the reflective sail, its flight time to these three rendezvous objects is close to or shorter than that of the reflective sail. In particular, the smaller the sail's area-to-mass ratio, the more obvious the advantage of the diffractive sail in the transfer time.

5 Case study and performance comparison

In this section, the optimal transfer solutions and control laws of the Sun-facing diffractive sail with the best deflection angle are evaluated and compared with the attitude-variable reflective sail for Mercury, Mars, and Apophis rendezvous missions.

5.1 Mercury rendezvous mission

Figures 10, 11, and 12 show the optimal transfer solutions of the most suitable diffractive sail with its corresponding best deflection angle at different acceleration capabilities and the reflective sail with the same area-to-mass ratio

Table 6 Comparison of the most suitable diffractive sail and the reflective sail for Apophis rendezvous mission

Sail type (best diffractive sail or ideal reflective sail)	ϵ (m^2/kg)	$\lvert\boldsymbol{a}_s\rvert$ (mm/s^2)	Best deflection angle (deg)	Transfer time (day)	(year)	Flight time difference (day)
High acceleration capability:						
Reflection-type diffractive sail	150	1.2743	41	367.7	1.007	+3
Ideal reflective sail	150	1.3605	—	364.7	0.999	—
Moderate acceleration capability:						
Reflection-type diffractive sail	50	0.3803	66	517.4	1.417	−14.9
Ideal reflective sail	50	0.4535	—	532.3	1.457	—
Low acceleration capability:						
Reflection-type diffractive sail	25	0.175	79	760.6	2.083	−58.2
Ideal reflective sail	25	0.2268	—	818.8	2.242	—

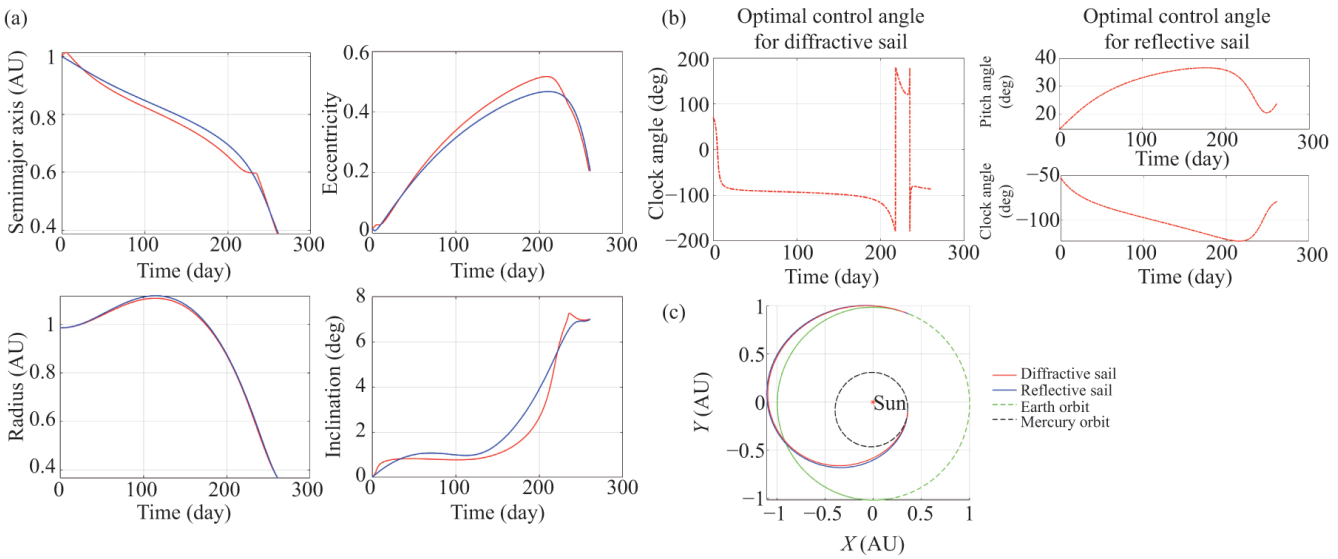

Fig. 10 High acceleration capability: Optimal transfer solutions of the most suitable diffractive sail (red line) and the reflective sail (blue line) with the same area-to-mass ratio of 150 m^2/kg for Mercury rendezvous mission. (a) Orbital elements over flight time. (b) Optimal control laws. (c) Optimal transfer trajectories.

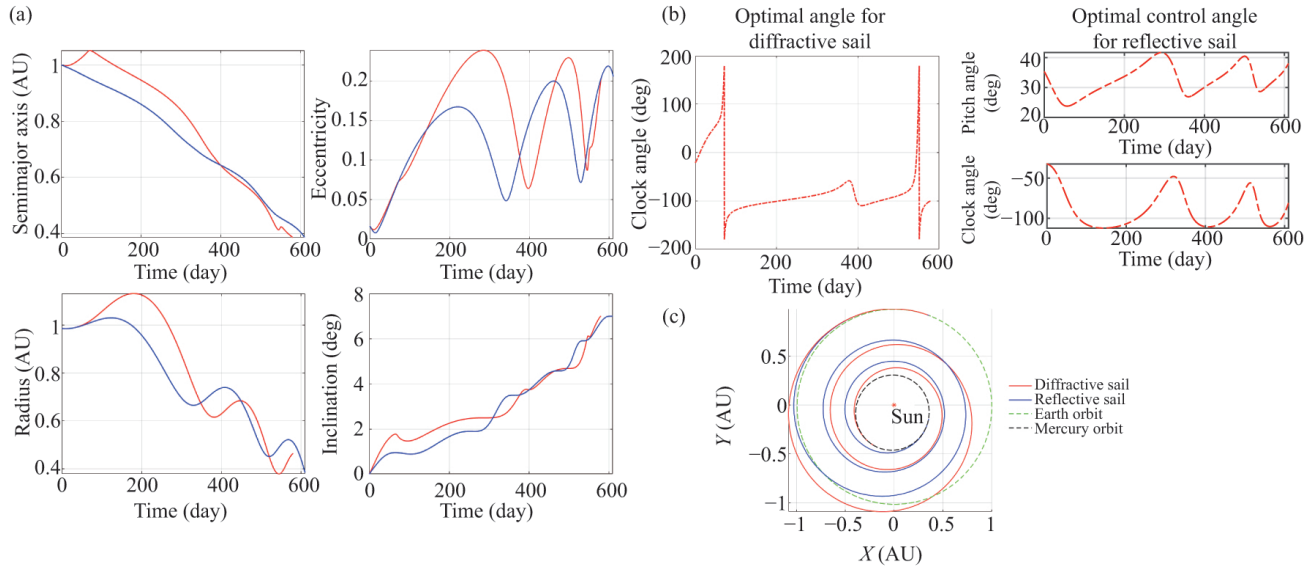

Fig. 11 Moderate acceleration capability: Optimal transfer solutions comparison of the most suitable diffractive sail (red line) and the reflective sail (blue line) with the same area-to-mass ratio of 50 m^2/kg for Mercury rendezvous mission. (a) Orbital elements over flight time. (b) Optimal control laws. (c) Optimal transfer trajectories.

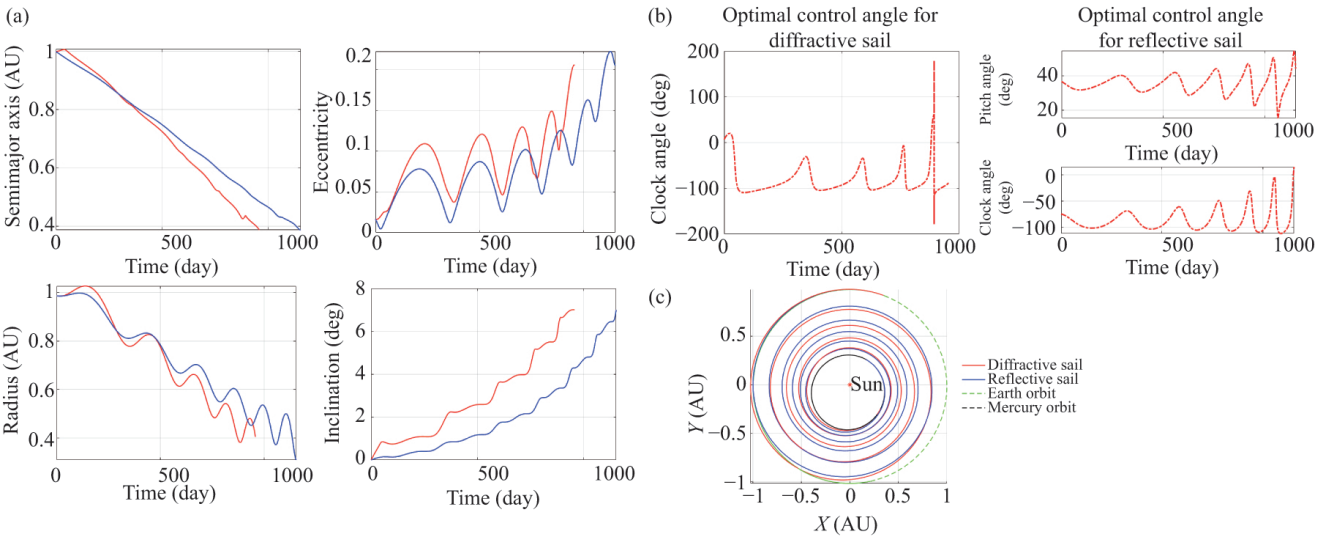

Fig. 12 Low acceleration capability: Optimal transfer solutions comparison of the most suitable diffractive sail (red line) and the reflective sail (blue line) with the same area-to-mass ratio of 25 m^2/kg for Mercury rendezvous mission. (a) Orbital elements over flight time. (b) Optimal control laws. (e) Optimal transfer trajectories.

from the Earth to Mercury.

As shown in Fig. 10, these two sails have similar transfer trajectories under high acceleration, allowing for a one-revolution transfer to Mercury. From the details, the eccentricity of the diffractive sail increases more rapidly in the beginning of the transfer, and the semimajor axis decreases more rapidly near the ending of the transfer, resulting in the slightly shorter transfer time than the reflective sail.

As shown in Fig. 11, the diffractive sail will first fly more outwards when it departs from the Earth to create a more elliptical transfer orbit with respect to the attitude-variable reflective sail. During the transfer process, the eccentricity of the diffractive sail also evolves more dramatically, which may benefit in shortening the transfer time.

As shown in Fig. 12, both the reflective sail and the diffractive sail require multiple loops to transfer to Mercury with an area-to-mass ratio of 25 m^2/kg, which is easily achievable. Compared with the attitude-variable

reflective sail, the eccentricity of the diffractive sail evolves more dramatically, resulting in a faster transfer orbit towards the Sun.

5.2 Mars rendezvous mission

Figures 13, 14, and 15 show the optimal transfer solutions of the most suitable diffractive sail with its corresponding best deflection angle at different acceleration capabilities and the reflective sail with the same area-to-mass ratio from the Earth to Mars.

As shown in Fig. 13, these two sails have similar transfer trajectories under high acceleration, allowing for a one-loop transfer to Mars. Compared with the reflective sail, the diffractive sail travels farther to reach Mars with longer transfer time. Note that the sail with high acceleration capability travels outward beyond Mars to match its end phase.

As shown in Fig. 14, at the beginning of the

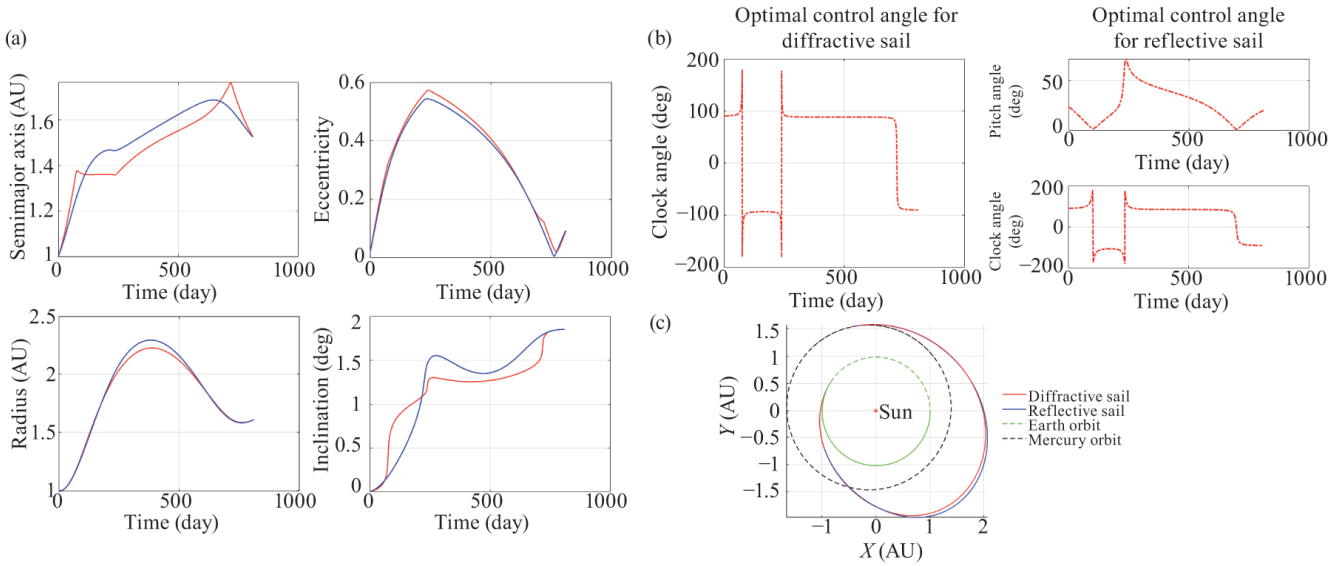

Fig. 13 High acceleration capability: Optimal transfer solutions comparison of the most suitable diffractive sail (red line) and the reflective sail (blue line) with the same area-to-mass ratio of 150 m^2/kg for Mars rendezvous mission. (a) Orbital elements over flight time. (b) Optimal control laws. (c) Optimal transfer trajectories.

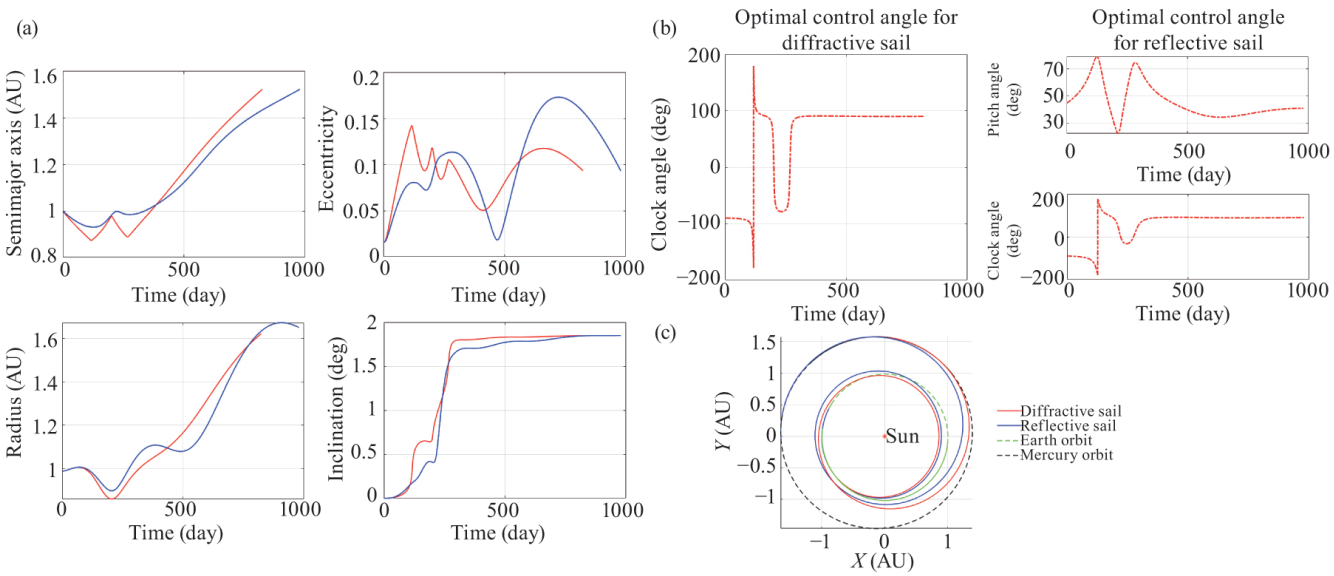

Fig. 14 Moderate acceleration capability: Optimal transfer solutions comparison of the most suitable diffractive sail (red line) and the reflective sail (blue line) with the same area-to-mass ratio of 50 m^2/kg for Mars rendezvous mission. (a) Orbital elements over flight time. (b) Optimal control laws. (c) Optimal transfer trajectories.

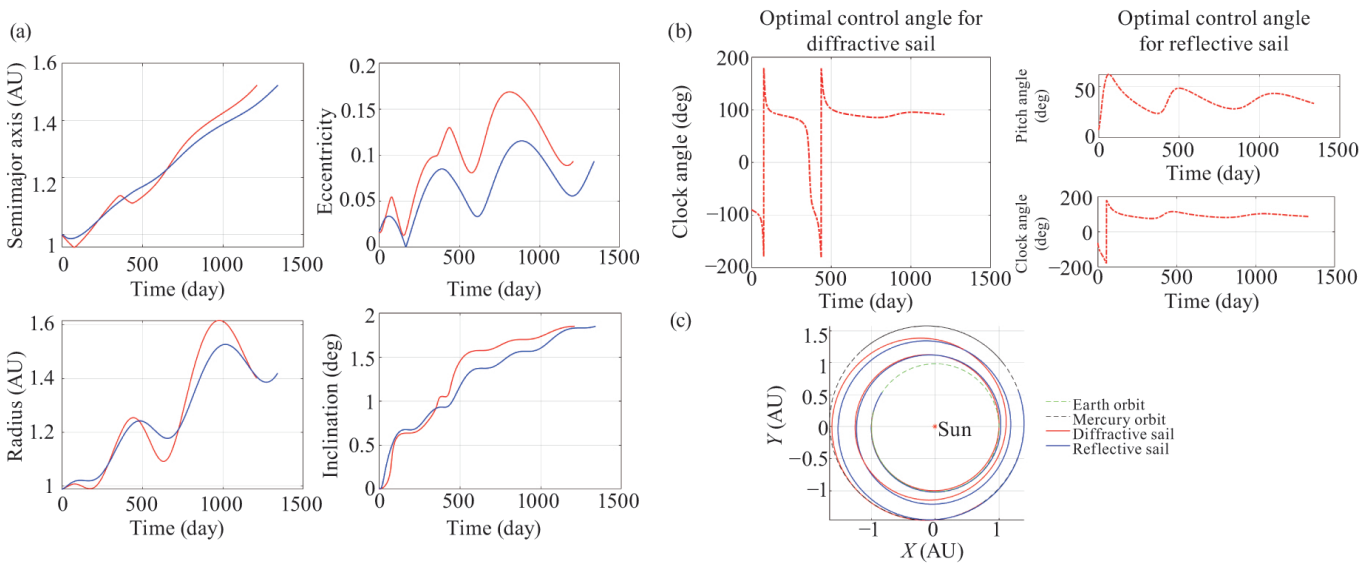

Fig. 15 Low acceleration capability: Optimal transfer solutions comparison of the most suitable diffractive sail (red line) and the reflective sail (blue line) with the same area-to-mass ratio of 25 m^2/kg for Mars rendezvous mission. (a) Orbital elements over flight time. (b) Optimal control laws. (c) Optimal transfer trajectories.

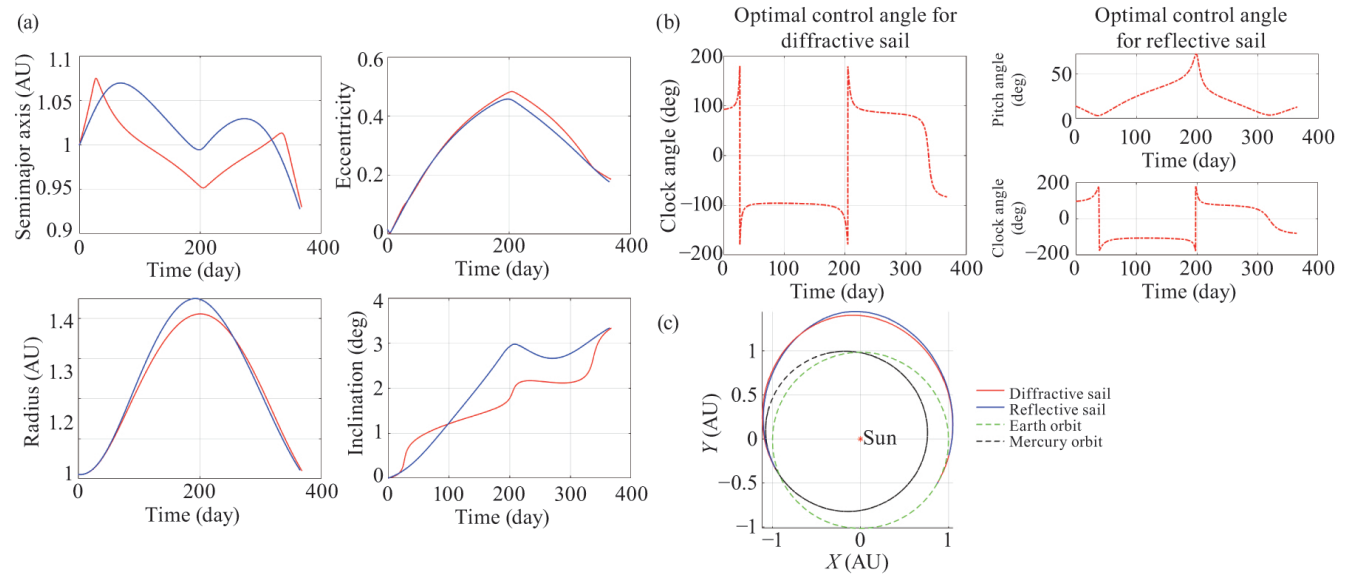

Fig. 16 High acceleration capability: Optimal transfer solutions comparison of the most suitable diffractive sail (red line) and the reflective sail (blue line) with the same area-to-mass ratio of 150 m^2/kg for Apophis rendezvous mission. (a) Orbital elements over flight time. (b) Optimal control laws. (c) Optimal transfer trajectories.

transfer, both sails move towards the Sun to enhance their maneuverability for flying outward. However, the diffractive sail can achieve a faster transfer to Mars by moving closer to the sun, which increases its maneuverability and creates a more elliptical transfer orbit.

As shown in Fig. 15, both the reflective sail and the diffractive sail require multiple loops to transfer to Mars with an area-to-mass ratio of 25 m^2/kg, which is easily achievable. Compared with the attitude-variable reflective sail, the diffractive sail has a more elliptical transfer orbit, resulting in a faster transfer orbit to Mars.

Additionally, from the optimal control laws of the diffractive sail and the reflective sail at the three acceleration capabilities from the Earth to Mars, we can see that the diffractive sail maintains a nearly constant clock angle at different stages of transfer, requiring quick adjustment only at stage junctions. In contrast, the pitch

angle of the reflective sail varies continuously during transfer, necessitating continuous attitude adjustments relative to sunlight.

5.3 Apophis rendezvous mission

Figures 16, 17, and 18 show the optimal transfer solutions of the most suitable diffractive sail with its corresponding best deflection angle at different acceleration capabilities and the reflective sail with the same area-to-mass ratio from the Earth to Apophis.

We can see that the transfer trajectories of the diffractive and reflective sail are similar for the Apophis rendezvous mission, regardless of their acceleration capabilities. Additionally, the optimal control laws for the diffractive sail's clock angle and the reflective sail's clock angle are also similar. However, the diffractive sail has an advantage over the reflective sail because it only needs to maintain a Sun-facing attitude during transfer,

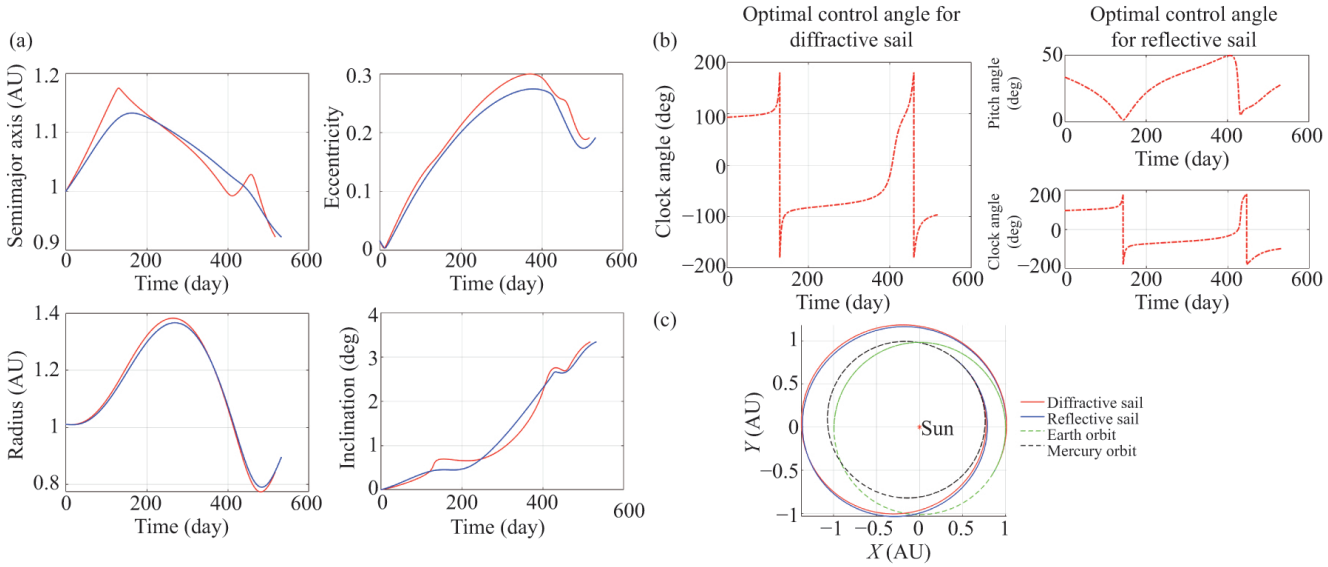

Fig. 17 Moderate acceleration capability: Optimal transfer solutions comparison of the most suitable diffractive sail (red line) and the reflective sail (blue line) with the same area-to-mass ratio of 50 m^2/kg for Apophis rendezvous mission. (a) Orbital elements over flight time. (b) Optimal control laws. (c) Optimal transfer trajectories.

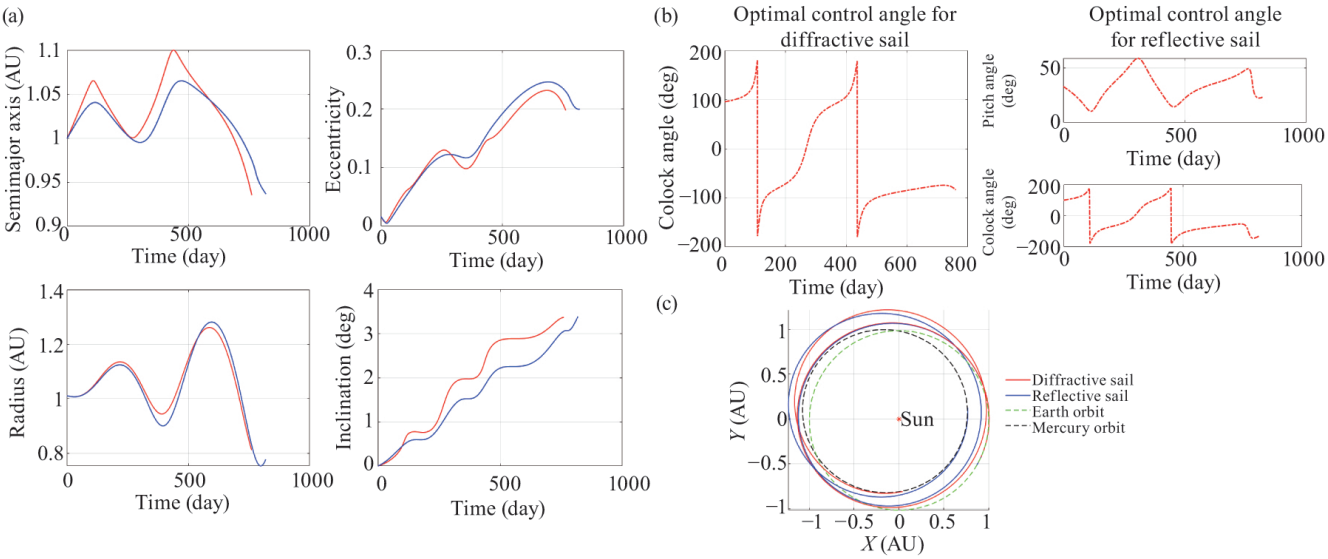

Fig. 18 Lowt acceleration capability: Optimal transfer solutions comparison of the most suitable diffractive sail (red line) and the reflective sail (blue line) with the same area-to-mass ratio of 25 m^2/kg for Apophis rendezvous mission. (a) Orbital elements over flight time. (b) Optimal control laws. (c) Optimal transfer trajectories.

while the reflective sail requires continuous adjustment of its pitch angle relative to sunlight, making the attitude adjustment process more complex.

6 Conclusions

In this paper, we examine the time-optimal rendezvous of Sun-facing diffractive sails with varied deflection angles, corresponding to different radiation pressure distributions. We consider both reflection and transmission types, establishing models for the orbital dynamics and radiation pressure accelerations of these sails with diverse deflection angles. The radiation pressure distributions and force characteristics of diffractive sails are thoroughly analyzed and compared to reflective sails.

Utilizing a mathematical model within a rectangular coordinate reference frame and an indirect method, we address the time-optimal control problem for Sun-facing diffractive sails in rendezvous missions, deriving the optimal control law for the clock angle. We then conduct numerical simulations of typical heliocentric rendezvous missions for Sun-facing diffractive sails with varying deflection angles and acceleration capabilities, comparing them to attitude-variable reflective sails.

Our simulation results indicate that high-acceleration-capability, reflection-type diffractive sails with deflection angles between 40 and 60 degrees exhibit superior transfer performance in near-in-plane heliocentric rendezvous missions. These missions include planetary rendezvous with considerable semi-major axis variations and near-earth asteroid rendezvous with significant eccentricity variations. This implies that substantial radial radiation pressure force can positively influence near-in-plane heliocentric rendezvous transfers.

However, as the acceleration capability of the diffractive sail decreases, the optimal deflection angle for the shortest transfer time increases, and the performance gap between reflection-type and transmission-type sails narrows in near-in-plane heliocentric rendezvous missions. This suggests that for lower acceleration sails, tangential radiation pressure force, which contributes to orbital normal and transverse accelerations, becomes increasingly important, while the impact of normal radiation pressure force on radial acceleration diminishes.

Compared to attitude-variable reflective sails, Sun-facing diffractive sails with appropriate deflection angles offer distinct advantages for near-in-plane heliocentric rendezvous missions, providing shorter transfer time and simpler attitude control, particularly when the sail's acceleration capability is limited.

We hope that this analysis and the derived conclusions can serve as valuable references for the design of future solar sails in specific rendezvous missions.

Acknowledgements

This work was supported by the National Natural Science Foundation of China (Grant No. 12372044). The authors would like to express sincere gratitude to Professor Grover A. Swartzlander, Jr. for his invaluable feedback and suggestions during the revision process of this paper. His insightful comments and constructive criticism have improved the quality of this work.

Declaration of competing interest

The authors have no competing interests to declare that are relevant to the content of this article. The author Shengping Gong is the Associate Editor of this journal.

References

[1] Friedman, L., Gould, M. Starsailing: Solar sails and interstellar space travel. *Physics Today*, **1988**, 41(5): 99.

[2] Vulpetti, G., Johnson, L., Matloff, G. L. *Solar Sails: A Novel Approach to Interplanetary Travel*. New York: Springer New York, **2015**.

[3] Mori, O., Tsuda, Y., Sawada, H., Funase, R., Yamamoto, T., Saiki, T., Yonekura, K., Hoshino, H., Minamino, H., Endo, T., Kawaguchi, J. World's first demonstration of solar power sailing by IKAROS. In: Proceedings of the 2nd International Symposium on Solar Sailing, **2010**: 19–20.

[4] Sawada, H., Mori, O., Okuizumi, N., Shirasawa, Y., Miyazaki, Y., Natori, M., Matunaga, S., Furuya, H., Sakamoto, H. Mission report on the solar power sail deployment demonstration of IKAROS. In: Proceedings of the 52nd AIAA/ASME/ASCE/AHS/ASC Structures, Structural Dynamics and Materials Conference, **2011**: AIAA 2011-1887.

[5] Mori, O., Shirasawa, Y., Mimasu, Y., Tsuda, Y., Sawada, H., Saiki, T., Yamamoto, T., Yonekura, K., Hoshino, H., Kawaguchi, J., *et al.* Overview of IKAROS mission. In: *Advances in Solar Sailing. Springer Praxis Books*. Berlin, Heidelberg: Springer Berlin Heidelberg, **2014**: 25–43.

[6] Nehrenz, M., Diaz, A., Svitek, T., Biddy, C. Initial design and simulation of the LightSail-1 attitude

determination and control system. In: Proceedings of the 2nd International Symposium on Solar Sailing, **2010**: 135–140.

[7] Spencer, D. A., Mansell, J. R., Betts, B., Bellardo, J. M., Diaz, A., Plante, B. The LightSail 2 controlled solar sailing demonstration mission. In: Proceedings of the 34th Annual Small Satellite Conference, **2020**: SSC20-II-01

[8] Johnson, L., Whorton, M., Heaton, A., Pinson, R., Laue, G., Adams, C. NanoSail-D: A solar sail demonstration mission. *Acta Astronautica*, **2011**, 68(5–6): 571–575.

[9] Davoyan, A. R., Munday, J. N., Tabiryan, N., Swartzlander, G. A., Johnson, L. Photonic materials for interstellar solar sailing. *Optica*, **2021**, 8(5): 722.

[10] Zeng, X. Y., Gong, S. P., Li, J. F. Fast solar sail rendezvous mission to near Earth asteroids. *Acta Astronautica*, **2014**, 105(1): 40–56.

[11] Quarta, A. A., Mengali, G. Solar sail missions to Mercury with Venus gravity assist. *Acta Astronautica*, **2009**, 65(3–4): 495–506.

[12] Gong, S. P., Baoyin, H. X., Li, J. Solar sail three-body transfer trajectory design. *Journal of Guidance, Control, and Dynamics*, **2010**, 33(3): 873–886.

[13] Gong, S. P., Gao, Y. F., Li, J. F. Solar sail time-optimal interplanetary transfer trajectory design. *Research in Astronomy and Astrophysics*, **2011**, 11(8): 981–996.

[14] Chu, Y., Wu, D., Gong, S. P. Enhanced transfer performance of Sun-facing diffractive sails in solar polar imager missions. *Advances in Space Research*, **2024**, 73(9): 4827–4841.

[15] Heiligers, J., Mingotti, G., McInnes, C. R. Optimal solar sail transfers between Halo orbits of different Sun-planet systems. *Advances in Space Research*, **2015**, 55(5): 1405–1421.

[16] Meras, A., Damaren, C. J. Using solar sails to transfer to the L5 Lagrange point. In: Proceedings of the AIAA Guidance, Navigation, and Control Conference, **2017**: AIAA 2017-1731.

[17] Farrés, A. Transfer orbits to L4 with a solar sail in the Earth–Sun system. *Acta Astronautica*, **2017**, 137: 78–90.

[18] Farres, A., Heiligers, J., Miguel, N. Road map to L4/L5 with a solar sail. In: Proceedings of the Space Flight Mechanics Meeting, **2018**: AIAA 2018-0211.

[19] Ancona, E., Kezerashvili, R. Y., Matloff, G. L. Exploring the Kuiper Belt with Sun-diving solar sails. *Acta Astronautica*, **2019**, 160: 601–605.

[20] Farrés, A., Heiligers, J., Miguel, N. Road map to L 4/L 5 with a solar sail. *Aerospace Science and Technology*, **2019**, 95: 105458.

[21] Sood, R., Howell, K. Solar sail transfers and trajectory design to Sun–Earth L4, L5: Solar observations and potential Earth Trojan exploration. *The Journal of the Astronautical Sciences*, **2019**, 66(3): 247–281.

[22] Song, Y., Gong, S. P. Solar-sail trajectory design for multiple near-Earth asteroid exploration based on deep neural networks. *Aerospace Science and Technology*, **2019**, 91: 28–40.

[23] Quarta, A. A., Mengali, G., Niccolai, L. Solar sail optimal transfer between heliostationary points. *Journal of Guidance, Control, and Dynamics*, **2020**, 43(10): 1935–1942.

[24] Niccolai, L., Quarta, A. A., Mengali, G. Solar sail heliocentric transfers with a Q-law. *Acta Astronautica*, **2021**, 188: 352–361.

[25] McInnes, C. R., McDonald, A. J. C., Simmons, J. F. L., MacDonald, E. W. Solar sail parking in restricted three-body systems. *Journal of Guidance, Control, and Dynamics*, **1994**, 17(2): 399–406.

[26] Baoyin, H., McInnes, C. R. Solar sail orbits at artificial Sun–Earth libration points. *Journal of Guidance, Control, and Dynamics*, **2005**, 28: 1328–1331.

[27] Baoyin, H., McInnes, C. R. Solar sail halo orbits at the Sun–Earth artificial L1 point. *Celestial Mechanics and Dynamical Astronomy*, **2006**, 94(2): 155–171.

[28] Baoyin, H., McInnes, C. R. Solar sail equilibria in the elliptical restricted three-body problem. *Journal of Guidance, Control, and Dynamics*, **2006**, 29: 538–543.

[29] Waters, T. J., McInnes, C. R. Periodic orbits above the ecliptic in the solar-sail restricted three-body problem. *Journal of Guidance, Control, and Dynamics*, **007**, 30: 687–693.

[30] Farrés, A., Jorba, À. A dynamical system approach for the station keeping of a solar sail. *The Journal of the Astronautical Sciences*, **2008**, 56(2): 199–230.

[31] Simo, J., McInnes, C. R. Solar sail orbits at the Earth–Moon libration points. *Communications in Nonlinear Science and Numerical Simulation*, **2009**, 14(12): 4191–4196.

[32] Farrés, A., Jorba, À. Periodic and quasi-periodic motions of a solar sail close to SL1 in the Earth–Sun system. *Celestial Mechanics and Dynamical Astronomy*, **2010**, 107(1): 233–253.

[33] Gong, S., Li, J., Simo, J. Orbital motions of a solar sail around the L2 Earth–Moon libration point. *Journal of Guidance, Control, and Dynamics*, **2014**, 37: 1349–1356.

[34] Gong, S. P., Li, J. F. Solar sail periodic orbits in the elliptic restricted three-body problem. *Celestial Mechanics and Dynamical Astronomy*, **2015**, 121(2): 121–137.

[35] Heiligers, J., Hiddink, S., Noomen, R., McInnes, C. R. Solar sail Lyapunov and Halo orbits in the Earth–Moon

three-body problem. *Acta Astronautica*, **2015**, 116: 25–35.

[36] Zeng, X. Y., Gong, S. P., Li, J. F., Alfriend, K. T. Solar sail body-fixed hovering over elongated asteroids. *Journal of Guidance, Control, and Dynamics*, **2016**, 39(6): 1223–1231.

[37] MacDonald, M., Hughes, G. W., McInnes, C. R., Lyngvi, A., Falkner, P., Atzei, A. Solar polar orbiter: A solar sail technology reference study. *Journal of Spacecraft and Rockets*, **2006**, 43(5): 960–972.

[38] Heiligers, J., Parker, J. S., MacDonald, M. Novel solar-sail mission concepts for high-latitude Earth and lunar observation. *Journal of Guidance, Control, and Dynamics*, **2018**, 41(1): 212–230.

[39] Thomas, D., Kobayashi, K., Mike, B., Bean, Q., Capizzo, P., Clements, K., Fabisinski, L., Garcia, J., Steve, S. Solar polar imager concept. In: Proceedings of the ASCEND, **2020**: AIAA 2020-4060.

[40] Dubill, A. L., Swartzlander, G. A. Circumnavigating the Sun with diffractive solar sails. *Acta Astronautica*, **2021**, 187: 190–195.

[41] Zeng, X. Y., Alfriend, K. T., Vadali, S. R. Solar sail planar multireversal periodic orbits. *Journal of Guidance, Control, and Dynamics*, **2014**, 37(2): 674–681.

[42] Zeng, X. Y., Vulpetti, G., Circi, C. Solar sail H-reversal trajectory: A review of its advances and applications. *Astrodynamics*, **2019**, 3(1): 1–15.

[43] MacDonald, M., McInnes, C. Solar sail science mission applications and advancement. *Advances in Space Research*, **2011**, 48(11): 1702–1716.

[44] Gong, S. P., MacDonald, M. Review on solar sail technology. *Astrodynamics*, **2019**, 3(2): 93–125.

[45] Spencer, D. A., Johnson, L., Long, A. C. Solar sailing technology challenges. *Aerospace Science and Technology*, **2019**, 93: 105276.

[46] Quarta, A. A., Mengali, G. Optimal solar sail transfer to linear trajectories. *Acta Astronautica*, **2013**, 82(2): 189–196.

[47] Niccolai, L., Quarta, A. A., Mengali, G. Analytical solution of the optimal steering law for non-ideal solar sail. *Aerospace Science and Technology*, **2017**, 62: 11–18.

[48] Oguri, K., Lantoine, G., McMahon, J. W. Solar sailing primer vector theory: Indirect trajectory optimization with practical mission considerations. *Journal of Guidance, Control, and Dynamics*, **2022**, 45(1): 153–161.

[49] Khabibullin, R. M. Spatial motion control algorithm of non-perfectly reflecting solar sail spacecraft for Earth–Mars flight. *AIP Conference Proceedings*, **2021**, 2318(1): 190006.

[50] Gorbunova, I., Starinova, O. An approach for the control method's determination for an interplanetary mission with solar sail. *AIP Conference Proceedings*, **2017**, 1798 (1): 020060.

[51] Caruso, A., Niccolai, L., Quarta, A. A., Mengali, G. Effects of attitude constraints on solar sail optimal interplanetary trajectories. *Acta Astronautica*, **2020**, 177: 39–47.

[52] Wie, B. Solar sail attitude control and dynamics, part 1. *Journal of Guidance, Control, and Dynamics*, **2004**, 27(4): 526–535.

[53] Lawrence, D., Piggott, S. Integrated trajectory and attitude control for a four-vane solar sail. In: Proceedings of the AIAA Guidance, Navigation, and Control Conference and Exhibit, **2005**: AIAA 2005-6082.

[54] Mettler, E., Acikmese, A., Ploen, S. Attitude dynamics and control of solar sails with articulated vanes. In: Proceedings of the AIAA Guidance, Navigation, and Control Conference and Exhibit, **2005**: AIAA 2005-6081.

[55] Hassanpour, S., Damaren, C. J. Collocated attitude and vibrations control for square solar sails with tip vanes. *Acta Astronautica*, **2020**, 166: 482–492.

[56] Romagnoli, D., Oehlschlägel, T. High performance two degrees of freedom attitude control for solar sails. *Advances in Space Research*, **2011**, 48(11): 1869–1879.

[57] Scholz, C., Romagnoli, D., Dachwald, B., Theil, S. Performance analysis of an attitude control system for solar sails using sliding masses. *Advances in Space Research*, **2011**, 48(11): 1822–1835.

[58] Huang, H., Zhou, J. Solar sailing CubeSat attitude control method with satellite as moving mass. *Acta Astronautica*, **2019**, 159: 331–341.

[59] Funase, R., Kanno, G., Tsuda, Y. Controllability of propellant-free attitude control system for spinning solar sail using thin-film reflectivity control devices considering arbitrary sail deformation. In: Proceedings of the International Astronautical Congress, **2012**: 6131–6138.

[60] Funase, R., Shirasawa, Y., Mimasu, Y., Mori, O., Tsuda, Y., Saiki, T., Kawaguchi, J. On-orbit verification of fuel-free attitude control system for spinning solar sail utilizing solar radiation pressure. *Advances in Space Research*, **2011**, 48(11): 1740–1746.

[61] Mashtakov, Y., Ovchinnikov, M., Petrova, T., Tkachev, S. Two-satellite formation flying control by cell-structured solar sail. *Acta Astronautica*, **2020**, 170: 592–600.

[62] Swartzlander, G. A. Radiation pressure on a diffractive sailcraft. *Journal of the Optical Society of America B*, **2017**, 34(6): C25.

[63] Srivastava, P. R., Chu, Y. L., Swartzlander, G. A. Stable diffractive beam rider. *Optics Letters*, **2019**, 44(12): 3082–3085.

[64] Swartzlander, G. A. Theory of radiation pressure on a diffractive solar sail. *Journal of the Optical Society of America B*, **2022**, 39(9): 2556.

[65] Swartzlander, G. A. Jr. Flying on a rainbow: A solar-driven diffractive sailcraft. *Journal of the British Interplanetary Society*, **2018**, 71: 130–132.

[66] Swartzlander, G. A., Lucy Chu, Y. J., Srivastava, P. R. Beam riders and sailcraft based on diffractive light sails. In: Proceedings of the Frontiers in Optics / Laser Science, **2018**: JTu2A.37.

[67] Chu, Y., Firuzi, S., Gong, S. P. Controllable liquid crystal diffractive sail and its potential applications. *Acta Astronautica*, **2021**, 182: 37–45.

[68] Firuzi, S., Gong, S. P. Refractive sail and its applications in solar sailing. *Aerospace Science and Technology*, **2018**, 77: 362–372.

[69] Firuzi, S., Song, Y., Gong, S. P. Gradient-index solar sail and its optimal orbital control. *Aerospace Science and Technology*, **2021**, 119: 107103.

[70] Bassetto, M., Caruso, A., Quarta, A. A., Mengali, G. Optimal steering law of refractive sail. *Advances in Space Research*, **2021**, 67(9): 2855–2864.

[71] Quarta, A. A., Mengali, G., Bassetto, M., Niccolai, L. Optimal interplanetary trajectories for Sun-facing ideal diffractive sails. *Astrodynamics*, **2023**, 7(3): 285–299.

[72] Quarta, A. A., Mengali, G. Solar sail orbit raising with electro-optically controlled diffractive film. *Applied Sciences*, **2023**, 13(12): 7078.

[73] Bassetto, M., Mengali, G., Quarta, A. A. Diffractive sail-based displaced orbits for high-latitude environment monitoring. *Remote Sensing*, **2023**, 15(24): 5626.

[74] Pontryagin, L. S. *Mathematical Theory of Optimal Processes*. Routledge, **2018**.

[75] Rao A. V. A survey of numerical methods for optimal control. In: Proceedings of the AAS/AIAA Astrodynamics Specialist Conference, **2009**: 497–528.

[76] Li, Z. C., Liu, W. W., Cheng, H., Chen, S. Q., Tian, J. G. Realizing broadband and invertible linear-to-circular polarization converter with ultrathin single-layer metasurface. *Scientific Reports*, **2015**, 5: 18106.

[77] Tabiryan, N. V., Serak, S. V., Nersisyan, S. R., Roberts, D. E., Zeldovich, B. Y., Steeves, D. M., Kimball, B. R. Broadband waveplate lenses. *Optics Express*, **2016**, 24(7): 7091–7102.

[78] Yu, N. F., Capasso, F. Flat optics with designer metasurfaces. *Nature Materials*, **2014**, 13: 139–150.

Yin Chu is a Ph.D. candidate of School of Aerospace Engineering, Tsinghua University. Her research interests include solar sailing, and constellation configuration maintenance. E-mail: chuy19@mails.tsinghua.edu.cn

Shenping Gong received his Ph.D. degree in mechanical engineering from Tsinghua University, China, in 2008. He is a professor at School of Astronautics, Beihang University. His research interests cover the rocket recovery guidance, solar sailing, dynamics of many-body system, and manned space flight. E-mail: gongsp@buaa.edu.cn